

Ultracool dwarfs identified using spectra in LAMOST DR7 [★]

You-Fen Wang¹, A-Li Luo^{1,2★★}, Wen-Ping Chen^{3,4★★★}, Hugh R. A. Jones⁵, Bing Du¹, Yin-Bi Li¹, Shuo Zhang^{6,7},
Zhong-Rui Bai¹, Xiao Kong¹, and Yan-Xin Guo¹

¹ CAS Key Laboratory of Optical Astronomy, National Astronomical Observatories, Beijing 100101, China.

² School of Astronomy and Space Science, University of Chinese Academy of Sciences, Beijing 100049, China

³ Graduate Institute of Astronomy, National Central University, 300 Zhongda Road, Zhongli, Taoyuan 32001, Taiwan

⁴ Department of Physics, National Central University, 300 Zhongda Road, Zhongli, Taoyuan 32001, Taiwan

⁵ School of Physics, Astronomy and Mathematics, University of Hertfordshire, College Lane, Hatfield AL10 9AB, UK

⁶ Department of Astronomy, School of Physics, Peking University, Beijing 100871, China

⁷ Kavli institute of Astronomy and Astrophysics, Peking University, Beijing 100871, China

Received September 00, 0000; accepted March 00, 0000

ABSTRACT

In this work, we identify 734 ultracool dwarfs with a spectral type of M6 or later, including one L0. Of this sample, 625 were studied spectroscopically for the first time. All of these ultracool dwarfs are within 360 pc, with a *Gaia* G magnitude brighter than ~ 19.2 mag. By studying the spectra and checking their stellar parameters (T_{eff} , $\log g$, and $[M/H]$) derived with the LAMOST pipeline, we found their cool red nature and their metallicity to be consistent with the nature of Galactic thin-disk objects. Furthermore, 77 of them show lithium absorption lines at 6708 Å, further indicating their young ages and substellar nature. Kinematics obtained through LAMOST radial velocities, along with the proper motion and parallax data from *Gaia* EDR3, also suggest that the majority of our targets are thin-disk objects. Kinematic ages were estimated through the relationship between the velocity dispersion and the average age for a certain population. Moreover, we identified 35 binaries, with 6 of them reported as binaries for the first time.

Key words. surveys:stars – late-type:stars – low-mass:brown dwarfs – binaries: visual

1. Introduction

Ultracool dwarfs (hereafter UCDs) are usually defined as objects with a spectral type of M7 V or later (Kirkpatrick et al. 1997), comprising very low-mass stars, brown dwarfs (BDs), and planetary-mass objects. The M7 V spectral type BDs are almost the highest-mass BDs that are just below the least mass stellar boundary. While the main-sequence stars, BDs, and planetary-mass objects are distinguished pedagogically by their masses, the mass values are not readily measurable. The luminosity and spectral type of a star, once core hydrogen fusion begins, remain effectively the same (depending on the mass) for hundreds of thousands to hundreds of million years on the main sequence. In contrast, for a substellar object, theoretical modeling indicates that – to use an example from Burrows et al. (1997) – a maximum-mass BD (about $75 M_J$) has a steady luminosity of $\log L/L_{\odot} \sim -1.3$ to $\log L/L_{\odot} \sim -2$ and an effective temperature of about $T_{\text{eff}} \sim 3000$ K for the first 10 Myr, then dropping to $\log L/L_{\odot} \sim -4$ and $T_{\text{eff}} \sim 2200$ K by the time the object be-

comes 1 Gyr old, corresponding to a spectral-type change from about an M6 to an L0. This age dependence on the spectral type makes it difficult to identify relatively massive and hot substellar objects. Thus, the class of late M to mid-L dwarfs represents a mixture of low-mass stars and BDs. Objects with ages later than mid-L spectral type are certainly BDs.

Brown dwarfs are objects that are not massive enough to sustain core hydrogen fusion, namely, they are substellar objects with masses of $M \lesssim 75\text{--}80 M_J$ (Marley et al. 2021), where M_J is the Jupiter mass. Theories indicate that the BDs with masses heavier than $\sim 65 M_J$ (Dantona & Mazzitelli 1985; Baraffe et al. 2015) have cores hot enough to fuse lithium – and those above $\sim 13 M_J$ may ignite deuterium. Other than these short-lasting fusion reactions, a BD continues to cool and fades monotonically in terms of brightness. Those with $M \lesssim 13 M_J$ have no fusion reaction at all and are called “planetary-mass objects” (or free-floating planets) that are in contrast to exoplanets orbiting host stars. The first M-type BD, an M8, was discovered by Rebolo et al. (1995) in the nearby cluster the Pleiades. In the same year, another BD of the T type (T6.5) was found by Nakajima et al. (1995), which is a companion to an M1 dwarf. These discoveries came 30 years after the theoretical prediction of BDs by Kumar (1963). Because of their intrinsic faintness, any optical spectroscopic vindication of a BD requires large-aperture tele-

[★] Tables 1 to 3 are only available in electronic form at the CDS via anonymous ftp to cdsarc.u-strasbg.fr (130.79.128.5) or via <http://cdsweb.u-strasbg.fr/cgi-bin/qcat?J/A+A/>

^{★★} Corresponding Author: A-Li Luo email: lal@nao.cas.cn

^{★★★} Wen-Ping Chen email: wpchen@ncu.edu.tw

scopes equipped with sensitive instruments. In spite of thousands of ultracool dwarfs proposed thus far, the key to true substellar nature by way of spectroscopic confirmation is possible only among nearby targets and – with dedicated efforts – in nearby star-forming regions.

Here, we present ultracool dwarfs with spectra types mainly ranging from M6 V to M9V that have been found with the Large Sky Area Multi-Object Fiber Spectroscopic Telescope (LAMOST, Luo et al. 2015). Thanks to a 4-m aperture and a 5-deg field of view to accommodate more than 4000 fibers on the focal plane, LAMOST is efficient in providing data for spectroscopic sky surveys. In this work, we examined a set of more than 10,000 spectra for objects with late M spectral type from the LAMOST DR7¹ (hereafter LDR7) and excluded the giants, those with low signal-to-noise (S/N) spectra or bad spectra, and those with earlier spectral types than M6 V. This list of ultracool dwarfs, while serendipitous in its sky coverage that is set by the LAMOST survey footprints, have been spectroscopically identified, therefore, expanding their currently known inventory of the ultracool population in the solar neighborhood considering the small population of late M dwarfs comparing with the early ones. This sample represents the low mass stars and bright brown dwarfs, which is crucial to understanding the physical process at the stellar and substellar boundary. It is also very useful for exoplanet surveys since they are much fainter than solar-like stars and, hence, it is easier to detect the low-mass rocky planets orbiting around them.

This paper is organized as follows. In Sect. 2, we describe the spectral data set used in this work and the procedure to select the ultracool dwarfs. In Sect. 3 we present the properties of the sample, such as the positions in the *Gaia* color-absolute magnitude diagram (CAMD), to verify their cool and red atmospheres. In Sect. 4, we diagnose the stellar parameters and compare them according to literature and we also inspect the possible existence of the lithium absorption line as an indication of the young age or substellar nature. In Sect. 5, we perform kinematic analysis using the radial velocity (RV) provided by LDR7 and the five astrometric parameters from the *Gaia* Early Data Release 3 (Gaia Collaboration et al. 2021a, hereafter GEDR3) to infer their stellar population and kinematical age. In Sect. 6, we report 35 binaries, of which 14 are newly discovered. Finally, we summarize our work in Sect. 7.

2. Data and sample selection

After the first light in 2008, commissioned in 2009–2010, followed by the Pilot Survey for one year (Luo et al. 2015), LAMOST had completed its five-year regular survey by June 2017. It is presently undertaking the second five-year regular survey. The latest data release, LDR7, includes low-resolution ($R \sim 1800$) spectra from which the stellar parameters were derived and which form the basis of the work reported here. With a practical LAMOST limiting sensitivity of *Gaia* $G \lesssim 19.2$ mag, our ultracool dwarfs were randomly observed in the footprints of the LAMOST survey, and the targets are randomly selected in any particular pointing within 5 square degrees. Information on the fiber assignment can be reviewed in (Luo et al. 2015). In this paper, we describe in detail on how to identify ultracool M dwarfs in LDR7 using spectral features.

2.1. LAMOST dataset

In order to construct our ultracool dwarf sample, we decided to set the cut at M6 to account for spectral typing uncertainties introduced in the LAMOST analysis pipeline (1 - 5 subtype depending S/N), as well as for spectral type dependence on age for BDs, so as not to exclude possible young BDs. In LDR7, 11,412 spectra were classified as being M6 or later by the LAMOST classification pipeline. Among these, about 33% are classified as dwarfs (listed as “dM” in the official catalogue) and 67% as giants (listed as “gM” in the official catalogue). In contrast, among early-type M spectra, only about 4% are found to be giants. The high fraction of giants at late-type M spectra type is attributed to the selection effect.

We cross-matched each of the 11,412 entries with the GEDR3 with a 5'' matching radius within the LAMOST coordinates (J2000). Firstly, 469 targets that pipeline classified as late-type M and have *Gaia* color BP-RP < 1 were removed because of a misclassification due to low spectra quality or data reduction. Secondly, we visually inspected all the spectra and winnowed out giants and early-type dwarfs via their spectral features, and we also excluded those having low signal-to-noise ratios. The remaining 734 targets are checked one by one to ascertain photometric counterparts to avoid mismatch caused by the multi-to-one problem, judged both by the positions and the colors of the 2MASS and the LAMOST targets. We further discuss the sample selection and present some details below.

2.2. Spectral features of giants versus dwarfs

A general description of the spectral features of M types in the LAMOST spectra can be reviewed in the work by Guo et al. (2015). Figure 1 illustrates the differences in spectral features between a typical dwarf and a giant with the same spectral type of M6. Prominent features for dwarfs include the K I doublets near 7688Å and Na I near 8189Å (Gray & Corbally 2009). The hydride band of CaH between 6800 and 7000Å is stronger in dwarfs than in giants; the bands for CrH and FeH around 8700 Å are visible in dwarfs. In comparison, giants have a more suppressed TiO absorption band to the red side of the Na I doublets and stronger Ca II triplets at 8498 Å, 8542 Å, and 8662Å. Moreover, giants exhibit a gentler slope between 8500 Å and 9000 Å compared to dwarfs that otherwise have molecular absorption due to TiO, VO, CrH, and FeH.

To select the sample of ultracool dwarfs, we applied visual inspection for all the 11,412 late M type spectra based on the above features, including both dwarfs (3764 dMs) and giants (7648 gMs) from the LDR7 official catalogue. After the inspection of the spectra, we found there are nine “real ultracool dwarfs” that had been misclassified as giants by the LAMOST pipeline and released in the giant catalogue; thus, we drew them back to our ultracool dwarf sample. For the LDR7 released dwarf sample, we excluded spectra with S/N lower than 2 in the z band, accounting for about four percent, as well as those of earlier M-type spectra that had been misclassified as late-type by the LDR7 pipeline. We also removed the spectra that have features between dwarfs and giants, namely, those with obviously weaker K I and Na I lines than classical dwarfs, such as YSOs, or those having features other than classical dwarfs (caused by data reduction, or being the mixture of two or multiple very close stars). Finally, we got an ultracool dwarf catalog of 734 sources, which is described in the following subsection. We should note that this

¹ <http://dr7.lamost.org>

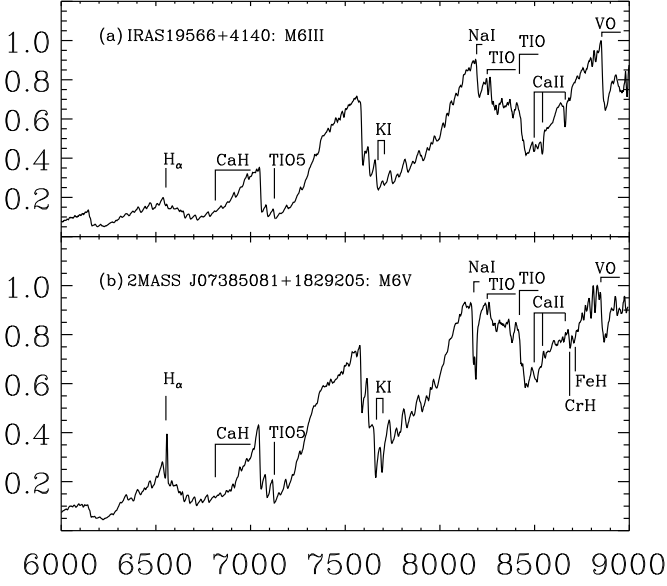


Fig. 1. Typical LAMOST spectrum of (a) an M6 III giant (Frasca et al. 2016), and (b) an M6 dwarf (Newton et al. 2014). Both spectra have S/N greater than 100 in the z band.

sample is conservative to ensure every source selected is indeed a real dwarf.

2.3. Sample of ultracool dwarfs

The visually identified 734 late-type M dwarfs have spectral type equal to or later than M6 V, with one L0 included. Figure 2 exhibits typical spectra of this sample. This sample is by no means complete in terms of sky coverage or flux but should form a reliable collection of the ultracool dwarf population in the LAMOST database. The observed spectra in our sample are consistent with the Hammer M dwarf templates, which have been established using the Sloan Digital Sky Survey (here after SDSS, Abazajian et al. 2009) optical spectra (Covey et al. 2007; Yi et al. 2014).

Table 1 lists the 734 ultracool dwarfs that we identified using LDR7 spectra, including 577 of the dM 6 and three gM 6, 128 of the dM 7 and two gM 7 type, 16 of the dM 8 and one gM 8 type, three of the dM 9 and three of the gM 9 type, and one of the L 0 type. Based on a cross-match with SIMBAD, we note that 625 out of the 734 objects had no spectral type listed in the literature prior to this work by LAMOST spectral observation.

The only one L dwarf, listed in Table 1 as No. 556, with the designation *SDSS* J120430.38+321259.4, has a SDSS spectral type of L0e in the optical (West et al. 2008) and M9.5 in the infrared (Bardalez Gagliuffi et al. 2014). It was observed in 2012 during the LAMOST pilot survey but was not included in the release until LAMOST DR6 because of its low brightness. This L0 dwarf indicates the practical limit of the latest spectral type in LDR7.

Figure 3 shows the sky distribution of the ultracool dwarfs (light purple solid circles) and the 11,412 LDR7 released late M type spectra (in green crosses), the background grey circles are the footprints (consist of more than 4900 plates each plate covers 5 square degrees) of the LDR7, covering about 20000 square degrees of the northern sky. In order to test the completeness and ratio of the red faint objects observed, we downloaded the data from GEDR3 in the sky area of LDR7 and

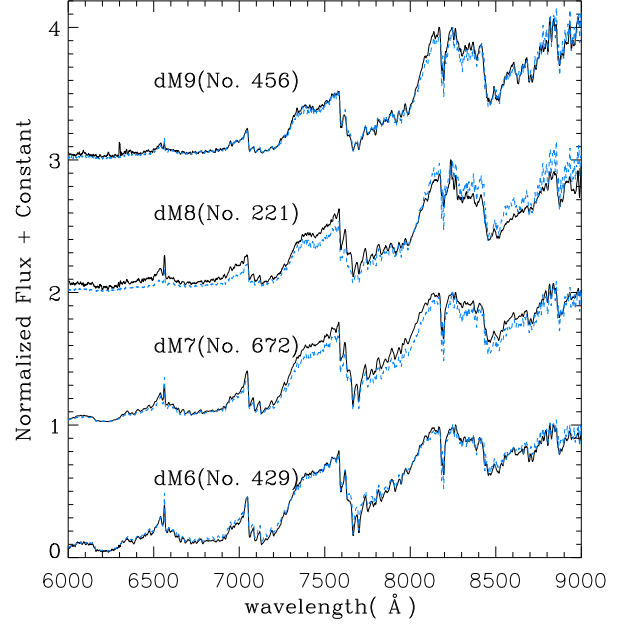


Fig. 2. Typical late-M dwarf LAMOST spectra (solid lines) in comparison to the Hammer template (blue dashed lines). Numbers given beside each spectral type corresponds to ID in Table 1. The S/N in SDSS z band for No. 429 \sim 70, No. 627 \sim 174, No. 221 \sim 30, No. 456 \sim 33.

obtained about 130 million Gaia sources. We then empirically estimated the number of the late-type M dwarfs by the color cut of *Gaia* $BP - RP > 3$ and apparent magnitude cut of $G < 19$, which result in 458 thousand objects. Using the absolute magnitudes of $G > 9$, we got 143 thousand candidates, accounting for 0.11% of the total. While for the approximately 10 million of the Gaia sources observed by LAMOST DR7, the pipeline classified 3,764 as late-type dMs, accounting for 0.03%, which means the very low portion of late dMs due to telescope magnitude limits. Although most of the LDR7 released late-type M dwarfs are correctly classified as real M type, many have low signal-to-noise ratio spectra or have fake spectral features. To avoid missing late dMs, we carefully check the spectral features for LAMOST released late dMs and gMs, and identified 734 relatively high S/N ultracool dwarfs later than M6, which ranging $5 > BP - RP > 2.63$ and absolute G magnitude between 8.94 and 16.71 (with relative parallax smaller than 20%). Since our ultracool dwarf sample is composed of good quality spectra and populated primarily with solar metallicity single stars, we can obtain more reliable atmosphere parameters and use them to update LAMOST classification templates.

3. GEDR3 photometry

The 11,412 late M spectra from LDR7 were cross-matched with the GEDR3 data within 5 arcsec as the previous section mentioned. In this section, we study the distribution of heliocentric distance and magnitude, $BP - RP$ versus $G - RP$ two-color diagram and CAMD diagram. Our ultracool dwarfs are very faint and red objects and represent the faintest stellar or substellar objects that LAMOST has ever observed. The heliocentric distance and *Gaia* magnitude distribution show the practical limitation of the LAMOST.

Table 1. Ultracool dwarfs in the sample

No.	obsid	R.A.	Decl.	SpT1	source_id	ϖ	$\Delta\varpi$	$\mu_\alpha \cos \delta$	$\Delta\mu_\alpha \cos \delta$	μ_δ	$\Delta\mu_\delta$	RUWE	G	G_{BP}	G_{RP}	SpT2
		(deg)				(mas)		(mas/yr)	(mas/yr)	(mas/yr)			(mag)	(mag)	(mag)	
1	369905116	0.29067	7.30335	dM7	2745889793400449280	25.43	0.15	135.18	0.19	-78.93	0.09	1.461	16.333	18.274	14.390	-
2	472904167	0.64809	17.48399	dM6	2772949702272966144	-	-	-	-	-	-	-	16.756	18.395	14.938	-
3	474610041	0.77652	39.20759	dM6	2881030840586539264	15.91	0.06	68.35	0.04	-56.65	0.04	1.009	16.574	18.716	15.222	-
4	592310145	1.82317	36.46536	dM6	2877146781401666816	14.19	0.07	16.77	0.08	-38.87	0.05	1.112	16.692	18.702	15.374	-
5	593009044	2.23202	49.31638	dM6	393621524910343296	67.76	0.04	352.67	0.03	202.42	0.03	1.103	14.385	16.769	12.998	-
6	472906086	2.45851	17.15581	dM6	2772737844422061440	28.13	0.07	-6.68	0.10	-77.52	0.08	1.005	16.340	18.788	14.941	-
7	354310106	4.60190	36.47204	dM6	2876595273240771840	20.78	0.05	174.36	0.04	-206.20	0.05	1.003	16.127	18.178	14.791	-
8	284610069	5.12607	33.08272	dM7	2863419584886542080	81.57	0.04	1075.61	0.04	-863.67	0.04	1.052	13.935	16.400	12.538	-
9	372110218	5.42199	36.32373	dM6	378382770487254912	10.47	0.11	-73.46	0.10	-26.90	0.10	1.726	16.640	18.522	15.275	-
10	614109230	6.12484	36.83748	dM6	378467643336605056	30.63	0.05	-132.67	0.04	-14.74	0.04	1.046	15.703	17.855	14.356	-
⋮	⋮	⋮	⋮	⋮	⋮	⋮	⋮	⋮	⋮	⋮	⋮	⋮	⋮	⋮	⋮	⋮

Notes. Column 1: running number. Column 2: LAMOST obsid. Columns 3-4: Right ascension(RA) and declination(Decl.). Column 5: LAMOST spectral type. Column 6: GEDR3 source_id. Columns 7-12: parallax, proper motion in R.A. and Decl. directions, and the corresponding uncertainty. Columns 13-15: *Gaia* G BP and RP magnitudes. Column 16: RUWE from GEDR3. Column 17: SpT from the literature according to SIMBAD. The electronic version of this table in entirety is available at http://paperdata.china-vo.org/YFW/aa_table1.csv

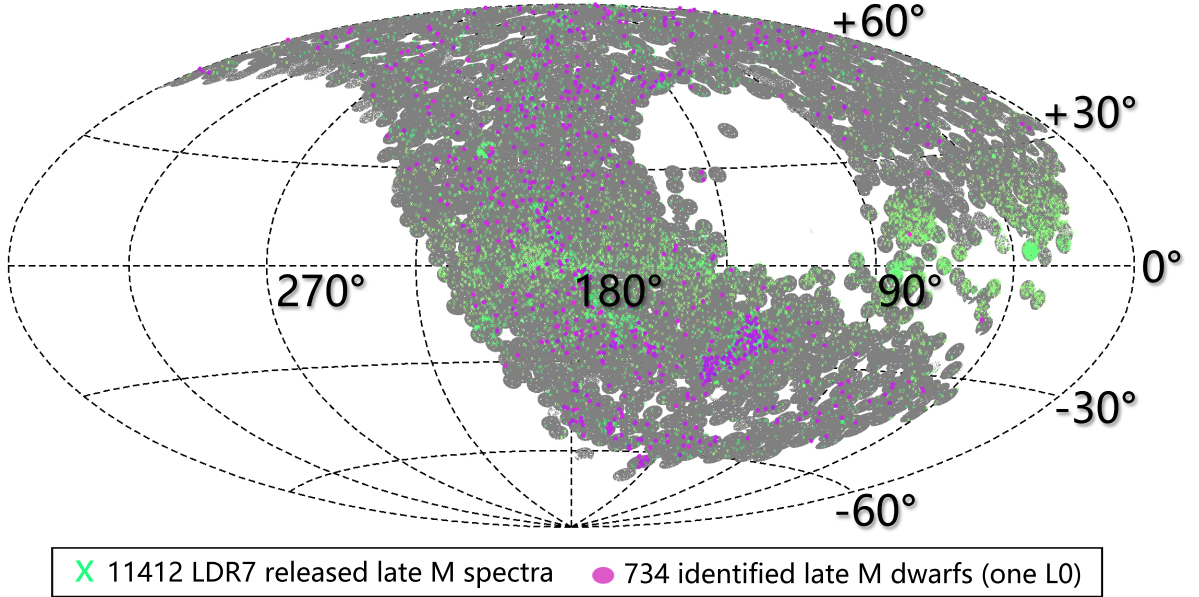


Fig. 3. Sky distribution of LAMOST DR7 released 11,412 late M stars (shown in green crosses), while the identified ultracool dwarfs are in light purple solid circles. The footprints for the LDR7 are plotted as grey big circles in the background.

To plot diagrams in this section, we restricted to objects with parallax that has relative uncertainty is smaller than 20% (Lutz & Kelker 1973; Luri et al. 2018), and that all *Gaia* G , BP , and RP values are greater than zero. The parallaxes of these ultracool dwarfs are large and hence expected to be nearby, we, therefore, adopted the reciprocal of the GEDR3 parallax as the distance of each source and thus determined their absolute magnitudes.

3.1. *Gaia* magnitudes and distance distribution

There are 677 of the ultracool dwarfs that meet the above mentioned requirements. The distance distribution is shown in Figure 4(a), with the ultracool dwarf sample in black solid lines. Figure 4(b) shows their *Gaia* G magnitude distribution.

Figure 4(a) indicates that the ultracool dwarfs are all within 360 pc. We notice that most of the ultracool dwarfs are within 100 pc ($\sim 83\%$). The G magnitude range is from ~ 12 to ~ 19.134 mag, the peak is at around ~ 16 mag – mean value of 16.206, corresponding to a spectral S/N measured in the equivalent SDSS z band S/N of 2 to 432 with a median of 61. We

note that our sample has spectra of good quality and is relatively convenient for model fitting or use as optical spectra templates.

3.2. Testing the sample with colors and absolute magnitude

Figure 5 (a) exhibits the CAMD of G absolute magnitude versus $BP - RP$, and (b) shows the two-color diagram of $G - RP$ versus $BP - RP$. For both (a) and (b) panels, the sources in Table 1 are in black solid circles, and the 11,412 LDR7 released late-type M from LDR7 are in cyan dots.

In Figure 5 (a), the main sequence, giant and white dwarf loci are obvious for the 11,412 late M from the LDR7. Our ultracool dwarf samples are all located in the bottom right corner – the loci of the reddest and coldest objects with $BP - RP$ between 2.63 and 5.00, G absolute magnitude between 8.94 and 16.71. It is reassuring to see that our ultracool dwarfs behave as expected, namely, they are consistent with being cool dwarfs. Although there seem to be white dwarfs below the upper main sequence among the 11,412 released late M objects, the case is not always true. There are eight sources located at the loci of the

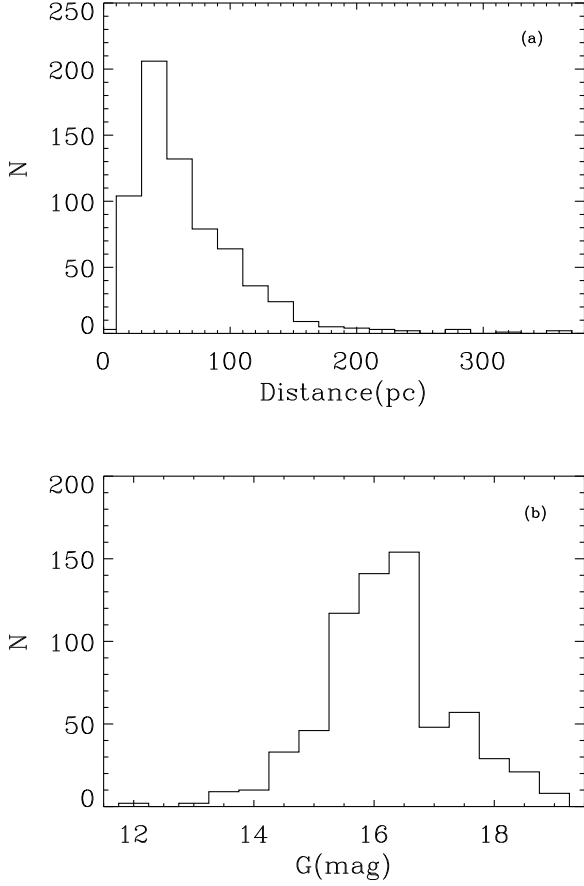


Fig. 4. Histograms of distance (panel a, reciprocal of the GEDR3 parallax, $\text{binsize} = 20$ pc), *Gaia* G magnitude (panel b, $\text{binsize} = 0.5$ mag).

white dwarf, but after checking their spectra, only three are DA white dwarfs and M dwarf binaries; whereas the other five do not show any obvious features of a white dwarf.

In panel (b), our ultracool dwarfs (black solid circles) locate at the top right – the red and cold loci as well, consistent with the Reylé (2018) on $G - RP$ color. However, the $G - RP$ color has greater uncertainties than the $BP - RP$ colors, presumably due to the relatively shorter color baseline of the $G - RP$ *Gaia* data. There are 49 sources with $G - RP$ greater than 1.5 when $BP - RP$ between 3 and 4.2, which is a fainter sub-sample with a mean G band magnitude of 16.825. They usually have RUWE (listed in table 1) value bigger than 1: the mean value is 3.28 and the median is 2.10. Greater RUWE values, that is, more than 1.4, indicates a significant possibility that there is an unresolved binary involved (Belokurov et al. 2020). The binary could be the cause of the peculiar $G - RP$ color. In Section 6.2, we show the $G - RP$ color for binaries in this paper. It is noteworthy that there are several high proper motion and wide separation binaries, which could lead to complexity and possible errors in the cross-matching process.

Our $BP - RP$ color appeared as expected, with normal distribution and without the problem Gaia Collaboration et al. (2021b) remarked for the case of UCDs (which have greater scatter on $BP - RP$ color caused by bigger uncertainty on BP magnitude due to their red and faint nature) since our sample is restricted to brighter sources. There are 533 of the ultracool sample re-

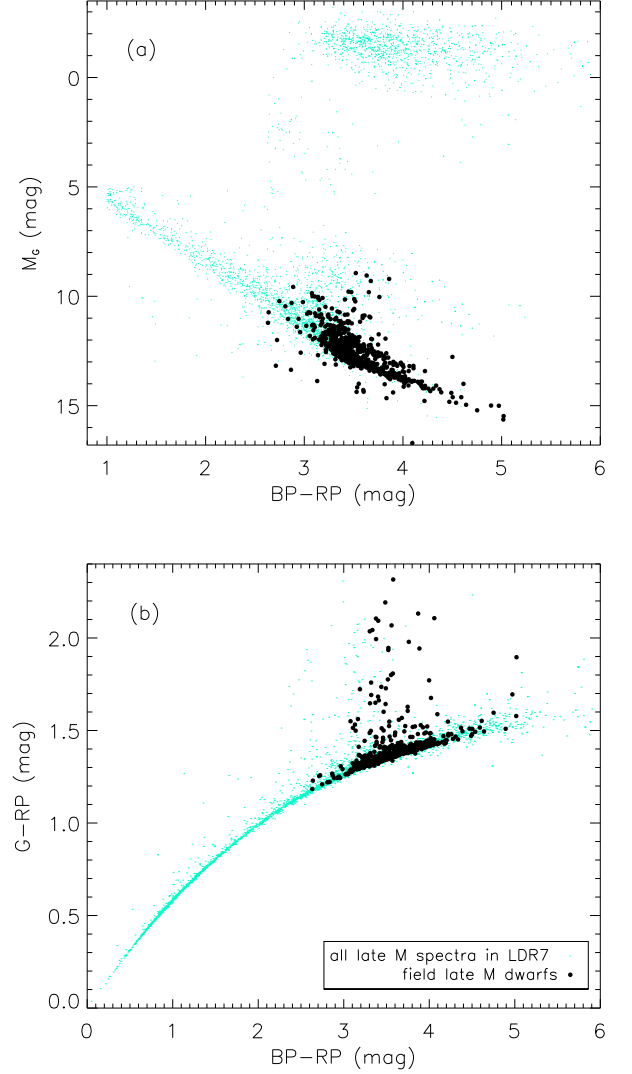


Fig. 5. (a) G absolute magnitude versus $BP - RP$ diagram. G absolute magnitude computed from the inverse of the parallax with no correction of extinction. The entire LAMOST DR7 late M sample is plotted in cyan dots, whereas the ultracool dwarfs are in black solid circles. (b) *Gaia* $G - RP$ versus $BP - RP$ color-color diagram. Symbols are the same as in the top panel.

ported in the work of Gaia Collaboration et al. (2021b), where they reported the nearby stars within 100 pc selected by the *Gaia* photometry and astrometry, and we report their spectral type in this work. Besides, our sample reported fourteen M6V to M8V which are predicted by Reylé (2018) using *Gaia* DR2 and 2MASS data. Skrzypek et al. (2016) and Ahmed & Warren (2019) reported 40,000 late-type M select by photometry, but only three objects in this sample overlap with our sample; this is probably because their samples are much fainter.

4. Spectroscopic analysis

Mass or age is needed to ascertain their sub-stellar nature and neither quantity is readily available. We hence relied on other criteria such as the T_{eff} , $\log g$, $[M/H]$ and strength of the lithium line, all available in the catalog and spectra of LDR7, as proxies of mass and age.

4.1. Atmospheric parameters

Stellar atmosphere parameters T_{eff} , $\log g$, and $[M/H]$ for M type objects in LDR7 are provided by LAMOST Stellar Parameter Pipeline for M stars (hereafter LASPM, Du et al. 2021). It minimizes χ^2 between the observed low-resolution spectra and a linear combination of five best-matching grids in the wavelength range of 6000 to 8800 Å with some specific contamination of the earth atmosphere masked (Du et al. 2021) to derive the stellar parameters. The LASPM does not provide stellar parameters for spectra with S/N in the SDSS i band below 5. The grids are from BT-Settle CIFIST2011 grids (Allard et al. 2011, 2012). The CIFIST2011 model is calculated from the radiative transfer code named “PHOENIX” with the solar abundance from Caffau et al. (2011), considering dust formation, gravitational settling, and convection. The line lists used are introduced briefly in Du et al. (2021). The coverage of T_{eff} , $\log g$ and $[M/H]$ are 300 to 8000K, 0.0 to 0.6 dex, and -2.5 to 0.5 dex with steps of 100 K, 0.5 dex, and 0.5, respectively.

The measured stellar parameters of the ultracool dwarfs are listed in Table 2. Letters “H, M, and L” in column 10 refer the first letter of “high,” “medium,” and “low,” indicating the strength of the lithium line, with “H” the strongest and “L” the weakest, based on visual checking of the lithium line. The label “N” indicates the absence of the lithium line. We did calculate the equivalent width, but it is a weak feature and the flux near 6708 Å is often rather noisy, so we do not report the value here.

We present the atmospheric parameters in Table 2. The effective temperature spread is from 2600 K to 3300 K, while the mean temperatures for each SpT are: M6 ~ 3018 K, M7 ~ 2917 K, M8 ~ 2775 K, and M9 ~ 2675 K. The mean temperatures cool down as the spectral type gets latter from M6 V to M9 V, and are roughly consistent with the literature that adopts atmospheric grid fitting with low or mid to high-resolution spectra (Rajpurohit et al. 2013; López-Valdivia et al. 2019) within 200K, but they are usually higher than the literature. We note there are only a few M8 and M9 dwarfs in both literature and our sample which makes the comparison difficult. If we make a comparison with the results of Reid & Hawley (2005) or Kaltenegger & Traub (2009), our mean temperatures are higher by about 350 K for each same SpT for late M dwarfs. One reason for this bias might be caused by the saturation of TiO absorption band in spectra later than M6. The TiO band is sensitive to temperature and weak for high temperatures, and then starts to saturate to the cool end (Passegger et al. 2016). This TiO behavior was not properly described in earlier versions of the PHOENIX models. The surface gravity varies from 3.5 to 5.5 dex with a mean of 4.43 dex. The measurement of surface gravity from the LASPM is broadly consistent with our expectations. And the metallicity varies from -0.99 to +0.38. The mean metallicity is $\langle [M/H] \rangle = -0.33$, consistent with Galactic disk dwarfs according to Wyse & Gilmore ($\langle [M/H] \rangle = -0.4$, 1995).

Thus, we give several cautions for our derived stellar parameters.

Firstly, the LASPM assumed the giants (with a spectral type of “gM”) have a surface gravity between 0 and 4.00 dex, while the dwarfs (with a spectral type of “dM”) have between 3.5 and 5.5. If a dwarf is misclassified as a “gM” it is likely this dwarf will have $\log g$ value that is smaller than 3.5. In our ultracool dwarf sample, there are 16 objects that have a surface gravity smaller than 3.5, but we checked their spectra and we know that they have prominent K I doublets near 7688Å, and Na I

near 8189Å. So, for these objects, we set their surface gravity at -9999.99.

Next, we know that LASPM assumed the giants (with spectral type of “gM”) have surface gravity between 0 and 4.00 dex, while the dwarfs (with a spectral type of “dM”) between 3.5 and 5.5. If a dwarf is misclassified as “gM,” it is likely this dwarf will have $\log g$ smaller than 3.5. In our ultracool dwarf sample, there are 16 objects that have surface gravity smaller than 3.5, but we checked their spectra and we know that they have prominent K I doublets near 7688Å, and Na I near 8189Å. So, for these objects, we set their surface gravity at -9999.99.

Lastly, although the values for the stellar parameters are statistically consistent with the expectations, it is better to check the spectra before adopting the parameters because LASPM, which is a pipeline aimed at compute parameters for a large number of objects, does not guarantee the accuracy of parameters for each individual object. In Table 2, the last two columns list the S/N for consideration.

4.2. Lithium diagnosis

Given the uncertainty in T_{eff} , $\log g$ and $[M/H]$, we did not attempt to estimate the mass of each of our ultracool dwarfs by connecting the atmospheric model to evolutionary ones. Instead, we can use a more direct proxy by looking for the presence of the lithium absorption line at 6708 Å. Given the low dispersion of the LAMOST DR7 spectra, we did not measure the equivalent width. Generally, the lithium test for BDs, including analysis of the equivalent width, requires an 8 to 10-meter telescope and mid-to-high dispersion spectroscopy (Rebolo et al. 1995; Martín et al. 1999; Kirkpatrick et al. 2008).

The lithium line for our ultracool dwarfs was checked. Figure 6 compares an ultracool dwarf showing the lithium line and another one without the lithium line, each with an inset zooming into the wavelength range about the lithium line at 6708 Å. In Table 2, as mentioned in the previous subsection, the 10th column labels “H/M/L” for the targets showing the lithium line, indicating the strength of high, medium, or weak, whereas “N” marks those with no detection of the line. There are 77 out of the 734 ultracool dwarfs with a prominent lithium absorption line at 6708 Å. We further explored the lithium line using the LAMOST single exposure spectra to exclude the impact of one bad single spectrum and to make sure that none of the above-mentioned lithium lines is caused by noise.

There is roughly 10% of our ultracool dwarf sample exhibiting the lithium feature, which is consistent with the study from Reiners & Basri (2009). The presence of a lithium line in a cool M dwarf with an age older than a few hundred Myr is firm evidence of mass below $65 M_J$, namely, below the hydrogen-burning limit; therefore, it is a brown dwarf (Reiners & Basri 2009). However, lithium depletion is expected to take about 100 Myr to reach completion. Definitive inference from the presence of lithium requires that reliable ages are established for all objects, which is not available especially for the field objects. Thus, it is safe to say that these 77 ultracool dwarfs are very probably brown dwarfs and that these lithium detections represent the first automated survey mode discoveries of lithium, establishing a significant new sample of lithium detections.

5. Kinematic diagnosis

Our ultracool dwarfs are all within 360 pc, namely, they are in the solar neighborhood and likely to be Galactic disk members.

Table 2. Radial velocity and atmosphere parameters in LDR7.

R.A.	Decl.	RV	T_{eff}	eT_{eff}	$\log g$	$e\log g$	[M/H]	$e[M/H]$	Li	S/N i	S/N z
(deg)	(deg)	(km s^{-1})	(K)	(K)	(dex)	(dex)	(dex)	(dex)			
0.29067	0.29067	11.85	2960	87	4.80	0.14	-0.20	0.10	N	80	106
0.64809	0.64809	-20.56	3045	87	4.21	0.15	-0.27	0.10	N	69	95
⋮	⋮	⋮	⋮	⋮	⋮	⋮	⋮	⋮	⋮	⋮	⋮
15.77892	15.77892	22.22	3053	108	4.61	0.17	-0.23	0.12	N	13	19
15.88307	15.88307	-25.09	3063	97	4.88	0.16	-0.18	0.11	N	78	97
15.93150	15.93150	3.06	3091	75	4.30	0.13	-0.23	0.09	N	84	110
15.93207	15.93207	3.51	3081	100	4.72	0.17	-0.09	0.12	N	63	79
16.16718	16.16718	-0.17	3004	105	4.87	0.17	-0.25	0.12	L	57	82
⋮	⋮	⋮	⋮	⋮	⋮	⋮	⋮	⋮	⋮	⋮	⋮

Notes. The parameters in LDR7. Columns 1-2: Position from LDR7 in epoch J2000. Column 3: RV. Column: 4-9: effective temperature, surface gravity, and metallicity, each parameter with their uncertainty followed. Column 10 label indicates if there is a lithium absorption line at 6708 Å by ‘‘H/M/L’’ (with the strength of the lithium at ‘‘H’’ as the highest level, ‘‘M’’ the medium, and ‘‘L’’ the weakest) or ‘‘N’’ (indicating no obvious lithium line). Columns 11 and 12: S/N in the SDSS i and z band. Here we show only a portion of this table, and it is published in its entirety in the online machine-readable format at http://paperdata.china-vo.org/YFW/aa_table2.csv

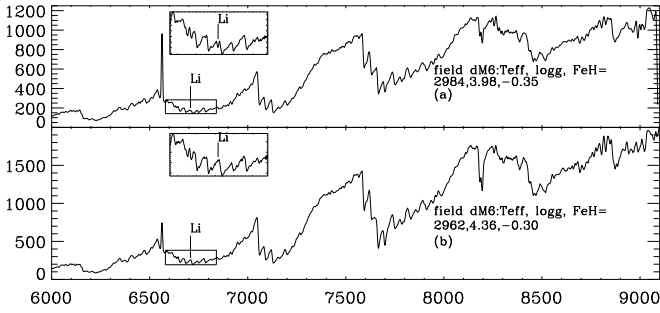


Fig. 6. Comparison of two spectra based on their 6708 Å lithium lines: One with the lithium line and another without. Panel (a) shows an M6 spectrum with a lithium absorption line. An M6 spectrum without lithium is shown in panel (b) for comparison. The small windows in each panel zoom in on the region that containing the 6708 Å lithium line. The atmosphere parameters from the LAMOST 1D pipeline are labeled.

However, there is a possibility that they may have a halo origin and will have a relatively high space velocity.

In this section, we study their kinematics. We calculate the UVW space motion and Galactic position using the RV (listed in Table 2) from LDR7 1D pipeline and the astrometric data from GEDR3. The position, namely, the Galactocentric distance and Galactic height, suggests that they are disk objects. With their LSR-corrected UVW velocity, we plotted our ultracool dwarfs on the Toomre diagram. In addition, we calculate the probability ratios of the thin-disk-to-thick-disk as well as that of the thick-disk-to-halo. In short, we conclude most of them are thin-disk objects. Using the thin-disk objects, we calculate the mean and scatter of the UVW velocities to infer their kinematic ages.

5.1. Space position and velocity

To ensure that the data we used are reliable, we excluded the data with relative uncertainty on parallax greater than 20%. Considering the RV, because of the typically broad spectral features and relatively poor S/N for M type spectra (especially for late M types) the RVs from low-resolution spectra provided by LDR7 for our ultracool dwarfs are potentially not reliable and we should exclude the unreliable RVs.

Thus, we measured the RV based on cross-correlation with M type spectral templates from Zhong et al. (2015) for compari-

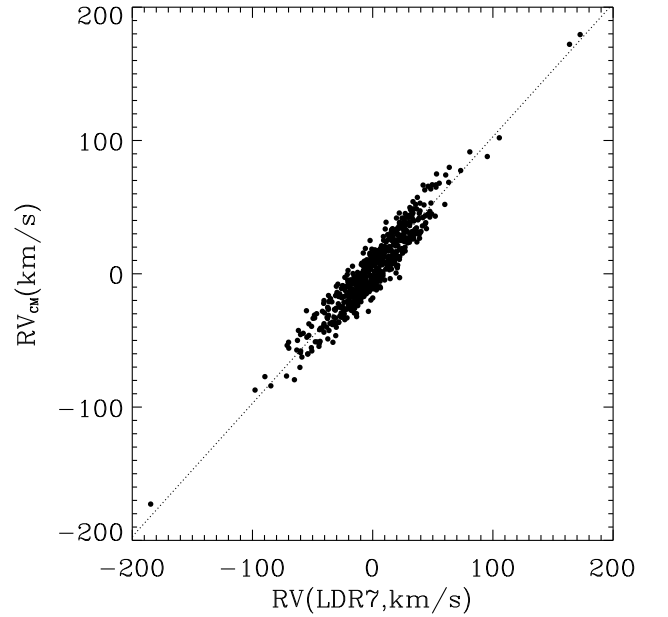


Fig. 7. Comparison of the LDR7 RV versus RV_{CM} after a 3 sigma clip on the residuals of the two sets of RVs. The x-axis is the LDR7 RV and y-axis RV_{CM} . The ultracool dwarfs in our sample are shown in black solid circles.

son with the RVs that come from LDR7. Our RV measurements are called RV_{CM} hereafter. Then we applied an iterative three-sigma clip to residuals of the two sets of RV to cut out unreliable RVs. Figure 7 shows the final RV comparison after iteration with a three-sigma clip. The x-axis is from LDR7 and the y-axis is from our RV_{CM} (in black solid circles) the standard deviation is 9.96 km s^{-1} . We adopted the LDR7 RV and 10% of RV for uncertainty, which is a relatively conservative value for uncertainty. The final adopted RV from LDR7 is consistent within three sigmas of RV_{CM} but the two RVs have an offset of about 3.0 km s^{-1} . After the exclusion of all unreliable measurements, there are 541 sources left in our sample.

Using the five GEDR3 astrometric parameters (R.A., Decl., proper motion, and parallax) and the LDR7 RV, the UVW space motion, then Galactocentric distance (R) and Galactic height (Z) are computed based on the following assumptions: 1) space mo-

tion with the U positive towards the Galactic center, V positive toward the Galactic rotation, and W positive to the Galactic north pole; 2) the distance between the earth and Galactic center is $R_{\odot} = 8.2$ kpc (Bland-Hawthorn & Gerhard 2016); 3) the motion of the local standard of rest (hereafter LSR) is 238 km s^{-1} , and velocity of the sun with respect to the LSR is $[U_{\odot}, V_{\odot}, W_{\odot}] = [14.0, 12.24, 7.25] \text{ km s}^{-1}$ (Schönrich et al. 2010; Schönrich 2012; Bland-Hawthorn & Gerhard 2016); and 4) the distribution of equatorial coordinates, proper motion, and parallax is a multivariate Gaussian (Marchetti et al. 2019; Li et al. 2021). The derived UVW , Galactocentric distance (R) and Galactic height (Z) are listed in Table 3.

5.2. Galactic population analysis

We show in Figure 8 the derived UVW velocities relative to the LSR and the Galactic position R and Z . The black solid circles indicate the objects in our sample, in panel (b), the blue squares show objects in binary systems. The Galactocentric distance and Galactic height are shown in plot (a). From this figure, their Galactic heights are between ~ -289 and $+229$ pc and the Galactic distances are between 8.1 and 8.5 kpc, which means they are the nearby local sample dominated by thin-disk objects. Further, we judge their Galactic membership using the Toomre diagram in plot (b) of Figure 8. The dashed lines in different colors are the total velocity limits between disk and halo from the literature. The green line indicates the thick-thin disk limit (Venn et al. 2004), the yellow and red are the thick disk-halo limit from Nissen & Schuster (2010) and Bonaca et al. (2017), respectively. Adopting either Nissen & Schuster (2010) or Bonaca et al. (2017), we see that the ultracool dwarfs are disk members in our sample and most of our sources are located within the thick-thin disk limit. There are 46 out of the 541 single objects located beyond the thin-thick disk limit but within the thick disk-halo limit; they are thick-disk objects, leaving 495 as thin-disk objects. The blue squares in Figure 8 panel (b) remind us of the binaries that we need to consider when doing further analysis in Section 5.3.

We studied the Galactic membership through thick-disk-to-thin-disk (hereafter TD/D) and thick-disk-to-halo (hereafter TD/H) probability ratios, which are calculated considering the distribution of thin-thick-halo components in velocity as well as the observed fractions of each population in the solar neighborhood following Bensby et al. (2003). The probability for each object is listed in Table 3. Two of our objects have the TD/H probability of 0.06 and 0.09 (less than 0.1), but according to their Galactic position (Figure 8), we conclude they are disk objects. Adopting a TD/D probability smaller than 0.1, 491 of the 541 objects are within the thin disk. In principle, the velocities of the objects in binary (as shown in Fig. 8) or multiple systems will be affected by their companions, so we did not include them in the following kinematic study. In Section 6, we further discuss these binaries.

We conclude that most of our ultracool dwarfs are thin-disk objects, while a small portion of them are thick-disk objects that are consistent with the metallicity analysis (see Section 4.1). In the next sub-section, we compute the UVW average value with respect to the Sun and the dispersion for our ultracool dwarfs, so as to estimate the kinematic age. For further study, we require the thin-disk objects to be judged as thin-disk stars by both the Toomre diagram and the probability ratio according to Bensby et al. (2003) method. There are 477 single thin-disk ob-

jects that meet our requirements. Correspondingly, there are 70 single thick-disk objects.

5.3. Velocity distribution and kinematic ages

Figure 9 shows the distribution of the UVW velocities for the thin-disk objects over-plotted with a Gaussian fit (in black) and the thick-disk ones (in dotted cyan bins). The binaries are not included in this figure to ensure that the objects shown are all singles to the best of our knowledge. We find that the velocities of the thin-disk objects in our sample have a prominent Gaussian profile and the velocity dispersion is very small. While for the thick disk components, the W velocity shows a prominent Gaussian peak in Figure 9 panel (c), but the distribution of U and W velocity does not look like a Gaussian distribution. This may be caused by the relatively small number of only 70 plotted. Hence, we did not carry out further kinematic analyses for the thick-disk objects in the following sections.

The mean and sigma of the UVW for singles (477 thin-disk objects) are presented below in Table 4. Our velocity data in this sub-section are heliocentric, so the average value of the sample reflects the anti-motion of the solar system relative to these dwarfs. Using our objects for reference, we find $(U, V, W)_{\odot} = [14.02^{+1.20}_{-1.21}, 17.60^{+0.71}_{-0.71}, 6.19^{+1.21}_{-1.20}] \text{ km s}^{-1}$; these average velocities agree within 3σ of previous literature results for the solar motion; for instance, Wang et al. (2018) studied the UVW velocity of about 200 L and T dwarfs, and found the solar motion of $(U, V, W)_{\odot} = [7.9 \pm 1.7, 13.2 \pm 1.2, 7.2 \pm 1.0] \text{ km s}^{-1}$. The U and W velocity of LSR we derived are consistent within 3σ with the adapted values in section 5.1: $(U, V, W)_{\odot} = [14.0, 12.24, 7.25] \text{ km s}^{-1}$ (Schönrich et al. 2010), while the V velocity is slightly bigger. The V_{\odot} is subject to controversies with the value varying from 1 to 21 km s^{-1} (Bovy et al. 2012; Robin et al. 2017; Gaia Collaboration et al. 2021b).

The standard deviation: $[\sigma_U, \sigma_V, \sigma_W] = [25.71^{+1.17}_{-1.18}, 18.53^{+0.89}_{-0.89}, 18.60^{+1.43}_{-1.37}]$ and total standard deviation: $\sigma_v = 36.75^{+4.21}_{-4.07}$ are all listed in Table 4. Our velocity dispersion is consistent with literature results that focus on BD samples, for instance, (23.0, 15.8, 12.2) from Wang et al. (2018), (25, 23, 20) km s^{-1} from Schmidt et al. (2010) and (30.2, 16.5, 15.8) km s^{-1} from Zapatero Osorio et al. (2007).

Our objects spend their time in a galactic potential which will vary and lead to dynamical evolution. A monotonic increase of velocity dispersion with age is seen for a given stellar population. We studied the kinematic age following the relationship between velocity dispersion and age given in Binney & Tremaine (2008):

$$\sigma_v(\tau) = v_{10} \left(\frac{\tau + \tau_1}{10 \text{ Gyr} + \tau_1} \right)^{\beta}, \quad (1)$$

where σ_v is the unweighted total velocity dispersion, and we used all six best-fit parameter sets of v_{10} , τ_1 and β in Table 2 of Aumer & Binney (2009) to provide an average age in (τ). With $\sigma_v = 36.75^{+4.21}_{-4.07} \text{ km s}^{-1}$, we find $\tau = 2.97^{+0.90}_{-1.06} \text{ Gyr}$ (listed in Table 4). This value is similar to the value of 3.1 Gyr for a sample of 63 late M dwarfs (Reiners & Basri 2009), but older than 1.7 Gyr for a sample of nearby L and T dwarfs (Wang et al. 2018) – consistent within 3σ for both values.

Table 3. Kinematic parameters.

R.A.	Decl.	U	V	W	Z	R	TD/D	TD/H
(deg)		(km s^{-1})			(pc)			
0.29067	0.29067	$-16.47^{+0.17}_{-0.17}$	$-14.41^{+0.69}_{-0.70}$	$-22.55^{+0.87}_{-0.98}$	$-6.58^{+0.19}_{-0.15}$	$8204.83^{+0.08}_{-0.09}$	0.01	5157
1.82317	1.82317	$12.80^{+1.34}_{-1.33}$	$-37.79^{+3.13}_{-3.08}$	$3.72^{+1.39}_{-1.64}$	$-5.34^{+0.13}_{-0.16}$	$8225.22^{+0.13}_{-0.13}$	0.01	4663
2.23202	2.23202	$-21.07^{+0.36}_{-0.41}$	$-17.74^{+0.83}_{-0.76}$	$11.62^{+0.19}_{-0.22}$	$21.71^{+0.01}_{-0.01}$	$8206.28^{+0.00}_{-0.00}$	0.01	4965
2.45851	2.45851	$8.02^{+0.14}_{-0.14}$	$-10.95^{+0.41}_{-0.40}$	$-4.75^{+0.43}_{-0.43}$	$0.07^{+0.06}_{-0.06}$	$8208.28^{+0.04}_{-0.04}$	0.01	5259
5.12607	5.12607	$-32.29^{+0.54}_{-0.52}$	$-60.11^{+1.06}_{-1.12}$	$-44.20^{+0.71}_{-0.67}$	$19.01^{+0.06}_{-0.00}$	$8204.61^{+0.01}_{-0.01}$	0.28	2186
⋮	⋮	⋮	⋮	⋮	⋮	⋮	⋮	⋮

Notes. The kinematic parameters. Columns 1-2 show the position from LDR7 in J2000, columns 3-5 are space motion $U V W$ with a unit of km s^{-1} . Columns 6-7 show the Galactic z and distance R with units in pc. The last two columns list the probability of Galactic membership, TD/D is the probability ratio of the thick disk to the thin disk, while TD/H indicates the probability ratio of the thick disk to the halo. Here is only a portion of this table, this table is published in its entirety in the online machine-readable format at http://paperdata.china-vo.org/YFW/aa_table3.csv

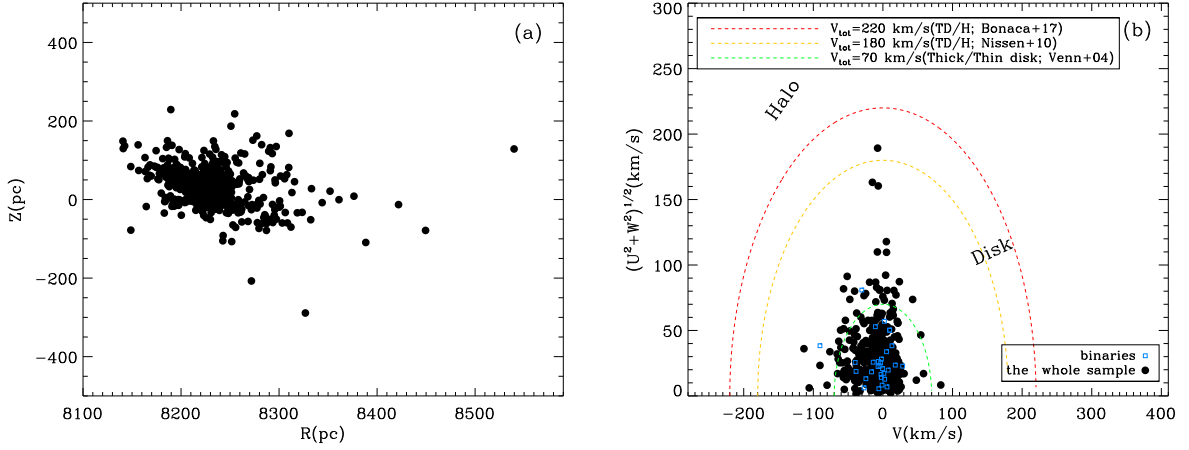


Fig. 8. Galactic R versus Z diagram (a). Toomre diagram for our objects (b). For both plots (a) and (b), our ultracool dwarfs are in black solid circles. The blue squares are objects in binary systems, The green dashed curve shows the thick-thin disk limit (Venn et al. 2004) of total velocity. The blue and yellow dashed curve indicates the thick and halo limit from Nissen & Schuster (2010) or Bonaca et al. (2017).

Table 4. Velocity distributions of thin-disk objects and their kinematic ages.

	$\langle v \rangle$	low err	high err	σ_v	low err	high err	Age	low err	high err
	(km s^{-1})	(Gyr)	(Gyr)	(Gyr)					
U	-14.03	1.20	1.20						
V	-17.60	0.71	0.71						
W	-6.19	1.21	1.20						
σ_U				25.71	1.17	1.18			
σ_V				18.53	0.89	0.89			
σ_W				18.60	1.43	1.37			
σ_{tot}				36.75	4.21	4.07			
Age							2.97	0.90	1.06

Notes. Distribution of the UVW velocity and their kinematic age.

6. Binaries in our sample

Among the sources in Table 1, one particular group deserves special attention: objects in binary systems. We study them using the GEDR3 and Pan-STARRS DR1 (here after PS1, Chambers et al. 2016) data. In this subsection, we report 35 “co-moving” binaries. The following subsections describe how we selected the binaries and carried out our analysis using the CAMD diagram, along with our literature search for previously reported binaries.

6.1. Identification of the binaries

Every source in Table 1 has been queried in GEDR3 for possible companions within an angular radius of $16''$. We then selected the systems with components comparable in proper motion and parallax; these are “common proper motion” binaries. We checked all images in PS1, but in Figure 10, we only present the PS1 images of six newly discovered binaries in this work and the eight newly discovered ones by Gaia Collaboration et al. (2021b). Table A.1 summarizes the properties of all our binaries. In this table, the first column is the identification number, with component “ a ” being the entry in Table 1, namely, having a LAMOST spectrum. Component “ b ” is the co-moving object in the system, with no implication of apparent bright-

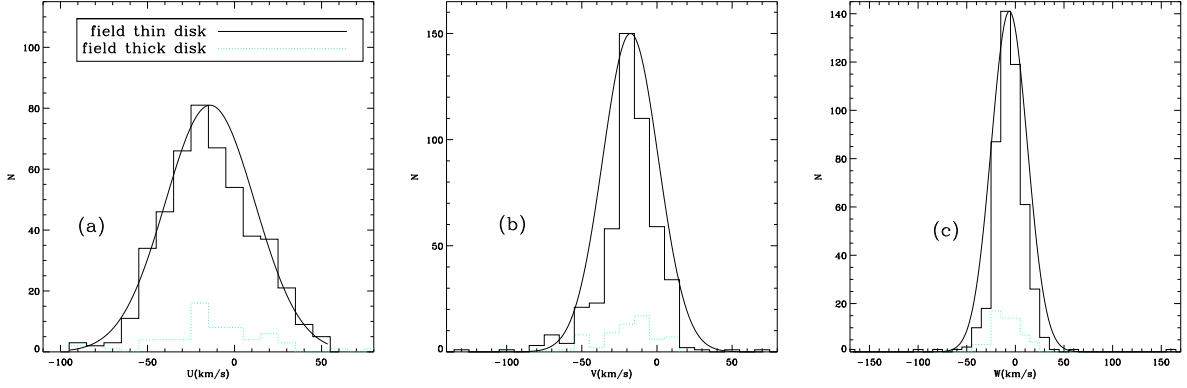


Fig. 9. Histograms of UVW velocities for the ultracool dwarfs. Objects in binary systems are deleted. Black solid histograms overlapped with the fitted Gaussian curve for the 477 thin-disk objects. Cyan dotted bars show the 70 thick-disk objects. Bin size is 10 km s^{-1} for all three panels.

ness or mass relative to the component “a.” Column 2 lists the GEDR3 source_id, with columns 3 and 4 being the coordinates in J2000 epoch computed the GEDR3 epoch J2016.0; Columns 5 to 10 list the GEDR3 G -band magnitude, parallax, proper motion, RUWE, and the angular separation (calculated using the positions in columns 3 and 4). Column 11 lists the references.

We note that the diameter of the LAMOST fiber is 3.3 arcsec and due to fiber packing, it is not feasible to target each component in a very close binary or multiple systems. We note that in this sample, every LAMOST object in Table 1 and its “companion” from the GEDR3 are resolved by GEDR3. But only the LAMOST “a” component in the pair was targeted by LAMOST, so its spectral type is known as listed in Table 1.

6.2. Positions in the CAMD

There are 35 binaries in total and 6 of them are newly discovered in this work, with images presented in Figure 10. Below, we show the positions for all of these binaries in the CAMD. With the magnitudes and parallaxes from the GEDR3, we studied the binaries in the CAMD. To plot the CAMD, we require the objects have relative uncertainty on a parallax better than 20% and G_{aia} G and G_{RP} magnitudes greater than zero.

In Figure 11, the black solid dots indicate the whole sample. While the blue squares indicate the LAMOST “a” components; the red triangles indicate the GEDR3 “b” components. The “a” and “b” components are connected using the dotted lines: there are 21 lines. The left 14 binaries have at least one component lacking a parallax or magnitude measurements from GEDR3, leading that only one component appears on this figure without lines connecting the two components. The dotted lines are largely parallel to the main sequence, which proves that they are coeval binaries, though some lines are far from the main sequence. There is one “b” component at the white dwarf loci: “26b”. The “26ab” is a known white dwarf-main-sequence binary reported by Tian et al. (2020). There are several lines not parallel to the main-sequence, which indicate that the components with significantly different colors might have different metallicities and ages. Besides, objects with redder colors and brighter magnitudes than the main sequence might be unresolved binaries.

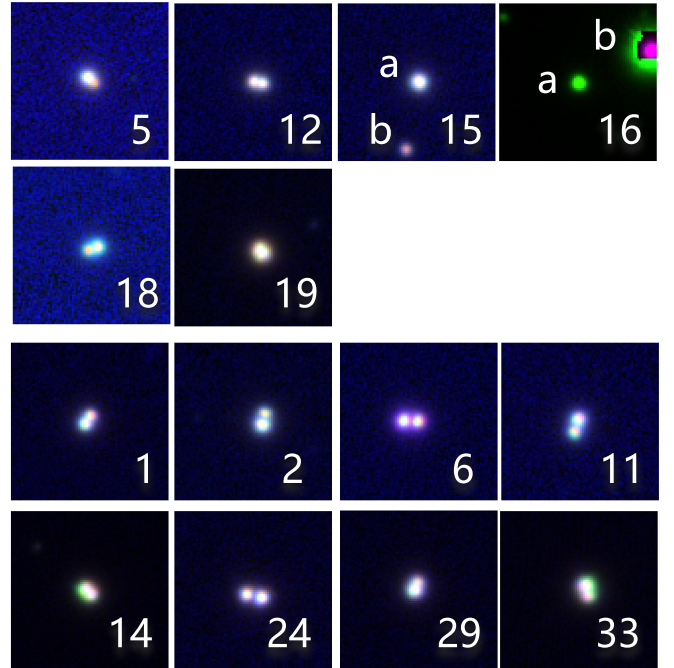


Fig. 10. PS1 $y/i/g$ band combined images for the 14 newly discovered binaries. The first two rows of images (labeled 5, 12, 15, 16, 18, and 19) show the binaries discovered directly in this work and the last two rows of images show those found by Gaia Collaboration et al. (2021b).

With north at top south at the bottom, west at right, and east at left. Their number IDs in Table A.1 are labeled in each frame. The scale is 20 arcsec for all these binary frames. The component “a” is always at the center of each image. The positions for the two components are labeled out in two frames (for those that have a wider separation).

6.3. Previously known systems

To search for known binaries, we first looked into the WDS catalog, the successor to the Index Catalogue of Visual Double Star, maintained by the United States Naval Observatory. The catalog provides parameters for double and multiple systems. There are 16 systems in Table A.1, already listed in the WDS catalog. Another binary catalog that we cross-matched with is the “Catalog of ultrawide binary stars from G_{aia} DR2” (Tian et al. 2020), in which we found seven of our binaries. The third cata-

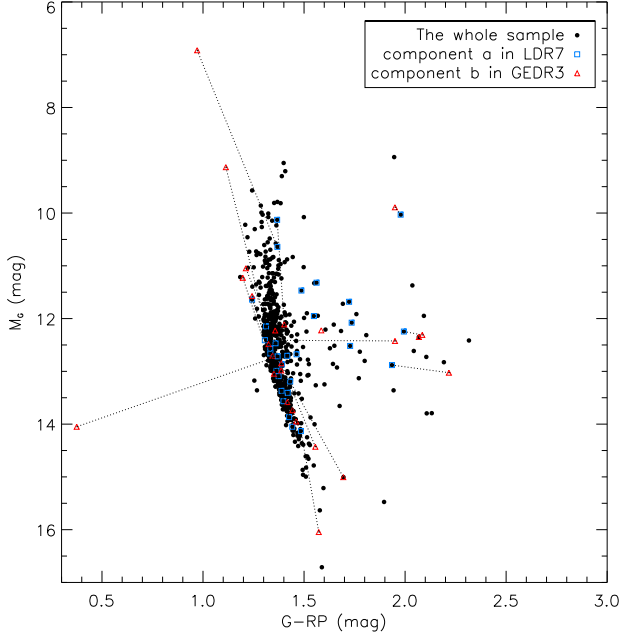


Fig. 11. CAMD in the *Gaia* photometry system for binary components. The x-axis is $G - G_{RP}$ and the y axis is absolute G magnitude. The legends at the top right describe the meaning of each symbol.

log we queried is the “SUPERWIDE Catalog” by Hartman & Lépine (2020), in which six of our binaries are listed. In the fourth catalog, we searched in Table 3 from *Gaia* Collaboration et al. (2021b), and found 19 of our binaries. In the literature, these are known as a “binary” that is worthy of attention for its particular properties.

System No. 21, known as *LP 213 – 67* and *LP 213 – 68*, has a rich record in the literature and might prove to be a quadruple system (Dupuy & Liu 2017). It was first discovered by Luyten & Hughes (1980) as a pair of ultracool dwarf (M6.5 for *LP 213 – 67* and M8 for *LP 213 – 68*), and later investigated by Close et al. (2003) using the AO system on Gemini to resolve the *LP 213 – 68*². Dupuy & Liu (2017), with a decade-long astrometric monitoring image from Keck Observatory, Hubble Space Telescope, and CFHT/WIRCam, suggested that *LP 213 – 68* may be a system with a main-sequence star having mass $\sim 97 M_{Jup}$ plus a BD $\sim 80 M_{Jup}$ with a ~ 2397 -day period. On the other hand, Konopacky et al. (2010) tried to use the Keck II 10 m telescope with the LGS AO system to derive the orbit and period for *LP 213 – 67*, but failed with insufficient epoch coverage. They provide a separation of $0''.032 \pm 0''.002$ and position angle of $\sim 126.77^\circ$ on 2006 Jun 21. A more detailed summary on *LP 213 – 67* and *LP 213 – 68* can be found in Dupuy & Liu (2017). We note that the “b” component of this binary system has a red color and brighter absolute G magnitude; furthermore, the RUWEs of the two components is greater than 1.4. The above color, absolute magnitude, and RUWE information could be indications of an unresolved binary for each individual component for other wide binary systems.

² Originally in Close et al. (2003), they reported an observation of *LP 213 – 67* but Dupuy & Liu (2017) found that the separation and position angle derived by Close et al. (2003) is much closer with their study on *LP 213 – 68* rather than the result of *LP 213 – 67* by Konopacky et al. (2010)

7. Summary

LAMOST DR7 released 11,412 spectra with the SpT equal to or later than M6, with both giants and dwarfs included. We visually inspected individual spectra according to spectral features and selected 734 ultracool dwarfs by excluding giants, misclassified early-type M dwarfs, and low S/N spectra. Based on the SIMBAD database, about 82% of the ultracool dwarfs have not been measured their spectral type before LAMOST.

We cross-matched all these 11,412 entries with the *GEDR3* within 5 arcsec and obtained their position on the CAMD with magnitudes and parallax of *Gaia*. We found that these samples show their correct locus as cool dwarfs on both the CAMD and the $BP - RP$ versus $G - RP$ diagram. The ultracool dwarfs are within 360 pc (83% of our ultracool dwarf sample are within 100pc) and brighter than 19.2 in *Gaia* G magnitude. The mean value of G band magnitude is around 16 mag.

We analyzed the stellar parameter measurements from LDR7. Effective temperature, surface gravity, and metallicity exhibit trends that are consistent with the literature expectation. Since these parameters are not calibrated for lacking sufficient external parameter estimation, it is important that individual spectra are checked before adopting the parameters. We did not estimate the mass for the ultracool dwarfs using stellar parameters and evolutionary tracks, but we checked the lithium line at 6708 \AA using the LAMOST low-resolution spectra. Overall, 10% of our ultracool dwarfs show a lithium absorption line, which is an indication of the young and substellar nature of ultracool dwarfs.

With the RV from LDR7 and astrometric data from GEDR3, we studied the Galactic membership of these ultracool dwarfs. From the Galactic position, Toomre diagram, and the probability ratio of thick-disk-to-thin-disk (TD/D) and thick-disk-to-halo (TD/H), we drew the same conclusion: they are all disk objects and most of them belong to the thin disk. This is consistent with the distances and metallicity distribution of LDR7. Using 477 thin-disk objects, we studied their UVW distribution. The mean and dispersion of the velocities are derived as $(U, V, W)_\odot = [14.02^{+1.20}_{-1.21}, 17.60^{+0.71}_{-0.71}, 6.19^{+1.21}_{-1.20}] \text{ km s}^{-1}$ and $[\sigma_U, \sigma_V, \sigma_W] = [25.71^{+1.17}_{-1.18}, 18.53^{+0.89}_{-0.89}, 18.60^{+1.43}_{-1.37}]$. The total standard deviation in velocity is $\sigma_v = 36.75^{+4.21}_{-4.07} \text{ km s}^{-1}$, corresponding to a kinematic age of $\tau = 2.97^{+0.90}_{-1.06} \text{ Gyr}$.

We found 35 common proper motion binaries and 6 of them are newly discovered binaries. Those with both parallax and magnitudes are shown on the CAMD: one literature source is known ultracool dwarf-white dwarf binary and its location is as expected. Furthermore, several binaries are shown to be coeval binaries and several of them appear to exhibit a peculiar color.

Acknowledgements. We thank Mr. Shih-Yun Tang for the idea of binarity study and help with *Gaia* data usage. We thank Dr. Richard L. Smart for a very useful discussion on the kinematic study of nearby cool objects. This work is supported by the National Key R&D Program of China (No. 2019YFA0405502), National Science Foundation of China (No U1931209), Chinese Space Station Telescope (CSST) pre-research projects of *Key Problems in Binaries and Chemical Evolution of the Milky Way and its Nearby Galaxies*. WPC acknowledges the financial support from the grant MOST 106-2112-M-008-005-MY3. HRAJ acknowledges support from a CAS PIFI Grant No. 2020VMA0033 and UK STFC grant ST/R006598/1. YXG acknowledges the National Science Foundation of China (Nos U2031137). YBL acknowledges the science research grants from the China Manned Space Project with NO.CMS-CSST-2021-A10, NO.CMS-CSST-2021-A08 and NO.CMS-csst-2021-B05.

Guoshoujing Telescope (the Large Sky Area Multi-Object Fiber Spectroscopic Telescope LAMOST) is a National Major Scientific Project built by the Chinese Academy of Sciences. Funding for the project has been provided by the National Development and Reform Commission. LAMOST is operated

and managed by the National Astronomical Observatories, Chinese Academy of Sciences.

References

- Abazajian, K. N., Adelman-McCarthy, J. K., Agüeros, M. A., et al. 2009, *ApJS*, 182, 543
- Ahmed, S. & Warren, S. J. 2019, *A&A*, 623, A127
- Allard, F., Homeier, D., & Freytag, B. 2011, in *Astronomical Society of the Pacific Conference Series*, Vol. 448, 16th Cambridge Workshop on Cool Stars, Stellar Systems, and the Sun, ed. C. Johns-Krull, M. K. Browning, & A. A. West, 91
- Allard, F., Homeier, D., Freytag, B., & Sharp, C. M. 2012, in *EAS Publications Series*, Vol. 57, *EAS Publications Series*, ed. C. Reylé, C. Charbonnel, & M. Schultheis, 3–43
- Aumer, M. & Binney, J. J. 2009, *MNRAS*, 397, 1286
- Baraffe, I., Homeier, D., Allard, F., & Chabrier, G. 2015, *A&A*, 577, A42
- Bardalez Gagliuffi, D. C., Burgasser, A. J., Gelino, C. R., et al. 2014, *ApJ*, 794, 143
- Belokurov, V., Penoyre, Z., Oh, S., et al. 2020, *MNRAS*, 496, 1922
- Bensby, T., Feltzing, S., & Lundström, I. 2003, *A&A*, 410, 527
- Binney, J. & Tremaine, S. 2008, *Galactic Dynamics: Second Edition*
- Bland-Hawthorn, J. & Gerhard, O. 2016, *ARA&A*, 54, 529
- Bonaca, A., Conroy, C., Wetzel, A., Hopkins, P. F., & Kereš, D. 2017, *ApJ*, 845, 101
- Bovy, J., Allende Prieto, C., Beers, T. C., et al. 2012, *ApJ*, 759, 131
- Burrows, A., Marley, M., Hubbard, W. B., et al. 1997, *ApJ*, 491, 856
- Caffau, E., Ludwig, H. G., Steffen, M., Freytag, B., & Bonifacio, P. 2011, *Sol. Phys.*, 268, 255
- Chambers, K. C., Magnier, E. A., Metcalfe, N., et al. 2016, arXiv e-prints, arXiv:1612.05560
- Close, L. M., Siegler, N., Freed, M., & Biller, B. 2003, *ApJ*, 587, 407
- Covey, K. R., Ivezić, Ž., Schlegel, D., et al. 2007, *AJ*, 134, 2398
- Dantona, F. & Mazzitelli, I. 1985, *ApJ*, 296, 502
- Du, B., Luo, A. L., Zhang, S., et al. 2021, *Research in Astronomy and Astrophysics*, 21, 202
- Dupuy, T. J. & Liu, M. C. 2017, *ApJS*, 231, 15
- Frasca, A., Molenda-Żakowicz, J., De Cat, P., et al. 2016, *A&A*, 594, A39
- Gaia Collaboration, Brown, A. G. A., Vallenari, A., et al. 2021a, *A&A*, 649, A1
- Gaia Collaboration, Smart, R. L., Sarro, L. M., et al. 2021b, *A&A*, 649, A6
- Gray, R. O. & Corbally, Christopher, J. 2009, *Stellar Spectral Classification*
- Guo, Y.-X., Yi, Z.-P., Luo, A. L., et al. 2015, *Research in Astronomy and Astrophysics*, 15, 1182
- Hartman, Z. D. & Lépine, S. 2020, *ApJS*, 247, 66
- Kaltenegger, L. & Traub, W. A. 2009, *ApJ*, 698, 519
- Kirkpatrick, J. D., Cruz, K. L., Barman, T. S., et al. 2008, *ApJ*, 689, 1295
- Kirkpatrick, J. D., Henry, T. J., & Irwin, M. J. 1997, *AJ*, 113, 1421
- Konopacky, Q. M., Ghez, A. M., Barman, T. S., et al. 2010, *ApJ*, 711, 1087
- Kumar, S. S. 1963, *ApJ*, 137, 1121
- Li, Y.-B., Luo, A. L., Lu, Y.-J., et al. 2021, *ApJS*, 252, 3
- López-Valdivia, R., Mace, G. N., Sokal, K. R., et al. 2019, *ApJ*, 879, 105
- Luo, A. L., Zhao, Y.-H., Zhao, G., et al. 2015, *Research in Astronomy and Astrophysics*, 15, 1095
- Luri, X., Brown, A. G. A., Sarro, L. M., et al. 2018, *A&A*, 616, A9
- Lutz, T. E. & Kelker, D. H. 1973, *PASP*, 85, 573
- Luyten, W. J. & Hughes, H. S. 1980, *Proper Motion Survey*, University of Minnesota, 55, 1
- Marchetti, T., Rossi, E. M., & Brown, A. G. A. 2019, *MNRAS*, 490, 157
- Marley, M. S., Saumon, D., Visscher, C., et al. 2021, *ApJ*, 920, 85
- Martín, E. L., Delfosse, X., Basri, G., et al. 1999, *AJ*, 118, 2466
- Mason, B. D., Wycoff, G. L., Hartkopf, W. I., Douglass, G. G., & Worley, C. E. 2001, *AJ*, 122, 3466
- Nakajima, T., Oppenheimer, B. R., Kulkarni, S. R., et al. 1995, *Nature*, 378, 463
- Newton, E. R., Charbonneau, D., Irwin, J., et al. 2014, *AJ*, 147, 20
- Nissen, P. E. & Schuster, W. J. 2010, *A&A*, 511, L10
- Passegger, V. M., Wende-von Berg, S., & Reiners, A. 2016, *A&A*, 587, A19
- Rajpurohit, A. S., Reylé, C., Allard, F., et al. 2013, *A&A*, 556, A15
- Rebolo, R., Zapatero Osorio, M. R., & Martín, E. L. 1995, *Nature*, 377, 129
- Reid, I. N. & Hawley, S. L. 2005, *New light on dark stars : red dwarfs, low-mass stars, brown dwarfs*
- Reiners, A. & Basri, G. 2009, *ApJ*, 705, 1416
- Reylé, C. 2018, *A&A*, 619, L8
- Robin, A. C., Bienaymé, O., Fernández-Trincado, J. G., & Reylé, C. 2017, *A&A*, 605, A1
- Schmidt, S. J., West, A. A., Hawley, S. L., & Pineda, J. S. 2010, *AJ*, 139, 1808
- Schönrich, R. 2012, *MNRAS*, 427, 274
- Schönrich, R., Binney, J., & Dehnen, W. 2010, *MNRAS*, 403, 1829
- Skrzypek, N., Warren, S. J., & Faherty, J. K. 2016, *A&A*, 589, A49
- Tian, H.-J., El-Badry, K., Rix, H.-W., & Gould, A. 2020, *ApJS*, 246, 4
- Venn, K. A., Irwin, M., Shetrone, M. D., et al. 2004, *AJ*, 128, 1177
- Wang, Y., Smart, R. L., Shao, Z., et al. 2018, *PASP*, 130, 064402
- West, A. A., Hawley, S. L., Bochanski, J. J., et al. 2008, *AJ*, 135, 785
- Wyse, R. F. G. & Gilmore, G. 1995, *AJ*, 110, 2771
- Yi, Z., Luo, A., Song, Y., et al. 2014, *AJ*, 147, 33
- Zapatero Osorio, M. R., Martín, E. L., Béjar, V. J. S., et al. 2007, *ApJ*, 666, 1205
- Zhong, J., Lépine, S., Li, J., et al. 2015, *Research in Astronomy and Astrophysics*, 15, 1154

Appendix A: Binaries

Table A.1. Binaries in the sample.

No.	source_id	R.A.	Decl.	G	ϖ	$\mu_{\alpha} \cos \delta$	μ_{δ}	RUWE	Sepa	LAMOST	REF
		(deg)	(deg)	(mag)	(mas)	(mas yr ⁻¹)			(arcsec)	(SpTy)	
1a	374266821724115840	14.60929	40.96502	16.563	10.562	65.447	-30.010	1.055	1.30	dM6	4
1b	374266821723253120	14.60905	40.96529	17.154	10.640	69.022	-29.769	0.866	-	-	4
2a	402667207072027008	16.21190	49.46696	16.265	10.983	-72.543	-48.021	1.121	1.50	dM6	4
2b	402667202774679808	16.21172	49.46733	17.297	10.916	-68.486	-48.482	0.948	-	-	4
3a	321982840504952448	19.87751	38.24850	17.648	11.075	0.015	-47.740	0.893	5.87	dM6	2;4
3b	32198284479985536	19.87646	38.24974	17.630	11.045	0.255	-48.071	1.011	-	-	2;4
4a	289697678714664320	20.60659	22.07549	16.098	18.790	-21.133	-11.048	1.209	7.33	dM6	3
4b	289697678714664192	20.60783	22.07711	14.670	18.848	-21.140	-12.270	1.026	-	-	3
5a	316277788200150400	24.21901	33.36533	17.688	7.123	46.367	-0.923	1.171	1.09	dM6	-
5b	316277788200960128	24.21876	33.36516	19.207	7.158	45.694	-1.860	1.022	-	-	-
6a	96492285755736448	25.81853	20.82407	16.421	17.828	144.663	-18.064	1.188	1.86	dM6	4
6b	96492285755202688	25.81801	20.82404	16.580	18.012	146.567	-14.172	0.883	-	-	4
7a	342530930417172224	29.08084	37.48177	15.929	22.216	203.994	-50.869	0.966	7.36	dM7	1;4
7b	342530930417172096	29.07952	37.48021	15.747	22.257	205.307	-49.469	1.166	-	-	1;4
8a	345777204139584384	29.50488	41.38132	15.137	30.660	-35.967	20.361	1.047	3.03	dM6	1
8b	345765453109062784	29.50516	41.38053	15.274	30.592	-34.291	23.813	1.209	-	-	1
9a	126144258931133568	39.74078	25.22135	14.728	30.488	208.525	-51.629	1.179	2.82	dM7	1;4
9b	126144258931133440	39.74023	25.22191	17.014	30.398	211.976	-49.911	1.156	-	-	1;4
10a	433763835445730944	42.96403	44.56884	14.782	-	-	-	-	8.63	dM6	1
10b	433763831149781376	42.96188	44.56989	15.413	32.648	145.710	-90.795	1.207	-	-	1
11a	3262741489171756160	50.45314	-0.86917	17.287	12.074	71.038	-109.761	0.971	1.55	dM6	4
11b	3262741489172243328	50.45300	-0.86876	16.806	12.117	74.970	-108.469	0.986	-	-	4
12a	216686773736734336	55.75914	32.12439	17.342	3.451	4.907	-6.991	1.033	1.24	gM9	-
12b	216686773735019264	55.75880	32.12433	17.324	3.262	4.859	-7.500	0.843	-	-	-
13a	3313784735944668544	66.91222	17.30882	15.627	9.768	19.060	-34.859	1.197	14.16	gM9	3
13b	3313784735944668032	66.91387	17.31239	13.162	9.561	19.384	-34.017	1.111	-	-	3
14a	3406246551375179392	71.25115	17.27227	16.194	16.229	69.710	-24.550	1.079	1.01	dM6	4
14b	3406246551373367168	71.25095	17.27208	16.225	16.471	70.797	-22.375	1.000	-	-	4
15a	3390528895217011712	79.88052	14.72899	16.591	5.100	-1.850	-8.109	1.164	8.74	dM6	-
15b	3390528890920404736	79.88102	14.72661	18.416	5.480	-1.689	-7.719	1.007	-	-	-
16a	3446362851590055808	82.80520	30.94254	16.556	6.561	3.024	-28.840	0.990	11.60	dM6	-
16b	3446362916013895552	82.80219	30.94369	12.644	7.148	5.606	-26.952	4.962	-	-	-
17a	3349802297332186496	89.32967	17.14099	15.428	48.737	233.929	-263.654	1.044	7.26	dM6	1;2;3;4
17b	3349805247975323392	89.32774	17.14157	12.785	48.804	242.615	-260.695	1.241	-	-	1;2;3;4
18a	884269552193012096	105.63858	27.68727	17.734	9.054	-34.352	-37.865	0.860	1.27	dM6	-
18b	884269552190985344	105.63892	27.68717	18.312	8.646	-34.871	-39.144	1.005	-	-	-
19a	3141512047219196672	113.14261	6.11010	16.784	14.341	-50.159	-33.730	1.037	0.75	dM6	-
19b	3141512051515263872	113.14247	6.10994	16.613	14.031	-46.712	-33.758	2.795	-	-	-
20a	660597997696173440	134.56281	19.76340	11.966	194.144	-767.060	-100.176	2.574	2.66	dM6	3
20b	660597997697274752	134.56311	19.76273	12.486	196.262	-937.133	-34.559	3.539	-	-	3
21a	779689606794219136	161.80254	40.44548	15.159	40.432	-298.288	-33.258	1.498	18.37	dM7	1;4
21b	779689533779300736	161.80740	40.44702	17.023	39.475	-301.661	-33.982	2.785	-	-	1;4
22a	3809562019331072384	162.94824	2.89455	15.647	35.030	-350.031	-56.090	1.011	3.53	dM7	1;4
22b	3809562019330343040	162.94878	2.89537	15.867	34.915	-342.425	-55.518	1.027	-	-	1;4
23a	729808234575686912	163.62886	25.96367	15.645	25.827	-85.038	-114.002	1.012	2.26	dM6	2;4
23b	729808230280106752	163.62946	25.96346	15.800	25.828	-90.340	-117.304	0.975	-	-	2;4
24a	3699132156679086720	181.09290	0.88691	16.980	13.642	93.048	-64.666	1.176	1.90	dM6	4
24b	3699132156679086848	181.09238	0.88680	16.624	13.189	93.822	-66.237	1.092	-	-	4
25a	4015042738059517440	185.36273	30.64324	13.383	83.504	-209.779	-267.270	0.926	5.32	dM6	1;2
25b	4015042738059517568	185.36136	30.64379	13.436	83.463	-191.036	-253.760	1.167	-	-	1;2
26a	4010091053083980032	186.44945	28.60449	17.268	12.288	-85.753	-259.333	1.057	17.51	dM6	3;4
26b	4010090670831602432	186.44531	28.60193	18.565	12.500	-87.315	-258.321	0.879	-	-	3;4
27a	4011353223713622528	189.36063	29.87850	16.547	20.354	-156.452	-102.041	1.000	10.98	dM6	1;2;3;4
27b	4011353223713630592	189.36366	29.87879	12.594	20.291	-156.509	-98.555	1.384	-	-	1;2;3;4
28a	1466583795164173184	198.02211	32.22596	16.053	18.687	113.194	-88.446	1.360	1.00	dM6	1;4
28b	1466583795162485120	198.02190	32.22578	16.073	18.623	112.014	-87.261	1.093	-	-	1;4
29a	3664079485466748288	207.56108	1.50458	16.384	13.764	57.639	-40.418	2.049	1.01	dM6	4
29b	3664079519825981056	207.56099	1.50484	17.223	13.431	54.726	-41.720	0.833	-	-	4
30a	3674243817630610304	212.46527	7.40705	15.128	35.534	-210.456	-36.320	0.704	1.38	dM6	1
30b	3674243817629910016	212.46545	7.40739	15.282	35.373	-222.378	-47.723	0.764	-	-	1
31a	1477762323724646272	214.94243	31.61928	15.442	52.662	104.455	-21.802	1.125	9.87	dM7	3
31b	1477762319428998400	214.94467	31.61770	12.962	52.747	99.281	-25.453	1.320	-	-	3
32a	1267909667590644992	225.58881	25.43186	18.204	15.332	-124.062	-54.785	1.128	9.02	dM7	2;4
32b	1267909671886228224	225.58885	25.43437	20.059	15.745	-123.180	-54.482	1.081	-	-	2;4
33a	1271532528341730176	228.43425	27.39515	15.559	14.194	-54.379	19.133	5.421	1.31	dM6	4
33b	1271532528339403648	228.43417	27.39480	16.390	14.219	-59.596	23.552	0.983	-	-	4
34a	1221808523727348480	232.99323	24.75628	17.206	7.709	-71.250	30.714	0.978	3.34	dM6	1;2
34b	1221808519429702784	232.99400	24.75679	19.335	7.591	-71.475	30.192	1.081	-	-	1;2
35a	2079073928612821760	298.47977	44.41504	11.908	214.574	349.363	-480.322	1.611	9.75	dM7	1
35b	2079074130463898624	298.47977	44.41233	11.535	-	-	-	-	-	-	1

Notes. Column 1 the identification(ID) number of the binaries, arranged in the order R.A. rising. Column 2: GEDR3 source_id. Columns 3-4: R.A. and Decl. in J2000(transferred from the GEDR3 epoch J2016.0). Columns 5-9: *Gaia* G band magnitude, parallax, proper motion, and RUWE from GEDR3. Column 10: Separation of the two components calculated using the position in columns 3 and 4. Column 11: References from 1-4: Mason et al. (2001); Hartman & Lépine (2020); Tian et al. (2020); *Gaia* Collaboration et al. (2021b). The six objects without a reference are newly discovered.